Available online at www.sciencedirect.com
ScienceDirect
Journal of Computational Physics 223 (2007) 551–570
JOURNAL OF COMPUTATIONAL PHYSICS
www.elsevier.com/locate/jcp

A numerical method for a second-gradient theory of incompressible fluid flow

Tae-Yeon Kim [a], John Dolbow [a,*], Eliot Fried [b]

[a] Department of Civil and Environmental Engineering, Duke University, Durham, NC 27708-0287, United States
[b] Department of Mechanical and Aerospace Engineering, Washington University in St. Louis, St. Louis, MO 63130-4899, United States

Received 5 April 2006; received in revised form 14 August 2006; accepted 21 September 2006
Available online 14 November 2006

Abstract

This work concerns the development of a finite-element method for discretizing a recent second-gradient theory for the flow of incompressible fluids. The new theory gives rise to a flow equation involving higher-order gradients of the velocity field and introduces an accompanying length scale and boundary conditions. Finite-element methods based on similar equations involving fourth-order differential operators typically rely on C^1-continuous basis functions or a mixed approach, both of which entail certain implementational difficulties. Here, we examine the adaptation of a relatively inexpensive, non-conforming method based on C^0-continuous basis functions. We first develop the variational form of the method and establish consistency. The method weakly enforces continuity of the vorticity, traction, and hypertraction across interelement boundaries. Stabilization is achieved via Nitsche's method. Further, pressure stabilization scales with the higher-order moduli, so that the classical formulation is recovered as a particular limit. The numerical method is verified for the problem of steady, plane Poiseuille flow. We then provide several numerical examples illustrating the robustness of the method and contrasting the predictions to those provided by classical Navier–Stokes theory.

PACS: 47.11.Fg; 47.11.–j; 47.85.Dh

Keywords: Finite-element; Non-conforming; Incompressible; Fluid; Second-gradient

1. Introduction

This work concerns a new finite-element method for discretizing a theory of incompressible fluid flow that incorporates length scale effects through the introduction of higher-order gradients of the velocity field. This "second-gradient" theory of fluid flow developed by Fried and Gurtin [4] was suggested as a means to describe behavior at length scales sufficiently small for deviations from classical Navier–Stokes theory to be conceivable. The theory fundamentally introduces two new moduli associated with length-scale effects in the bulk and near boundaries, and may also prove useful to describe flows over "rough" surfaces. A strong connection

* Corresponding author.
E-mail address: jdolbow@duke.edu (J. Dolbow).

0021-9991/$ - see front matter © 2006 Elsevier Inc. All rights reserved.
doi:10.1016/j.jcp.2006.09.022

to the Lagrangian averaged Navier–Stokes-α (LANS-α) model of turbulence was later made by Fried and Gurtin [5]. To date, only analytical solutions to simple model problems have been examined for the second-gradient theory. The objective of this work is to advance a numerical method based on finite elements, such that the predictions and applicability of the theory can be more fully examined.

The origins of the second-gradient theory of fluid flow can be traced back to Gurtin [1], who developed general balance equations and associated boundary conditions for a "second-grade material" using a non-standard form of the principle of virtual power. Gurtin's work generalizes the early results provided by Toupin [2,3], who developed analogous conditions for an elastic body whose strain energy depends on first and second gradients of the deformation. The main contribution of Gurtin's work is that it is independent of constitutive assumptions. As such, it is equally applicable to fluids as solids. Fried and Gurtin [4] recently adapted this framework to develop a theory of fluid flow incorporating higher-order gradients of the velocity field. Subsequently, Fried and Gurtin [5] established a connection to the LANS-α model. The LANS-α model of turbulence confers several advantages over LES and Reynolds averaged models, including the preservation of non-linear coherent structures (see the work of Holm et al. [6] for a synopsis). Aside from an extension of the Navier–Stokes equation involving higher-order gradients of the velocity field and involving an accompanying length scale, the framework of the second-gradient theory provides consistent boundary conditions on free and fixed boundaries. The free boundary conditions involve the curvature of the free surface; among the conditions for a fixed boundary are generalized adherence and slip conditions, each of which involves a material length scale.

Our current interest is focused on examining further the predictions that this second-gradient theory for fluid flow provides. Accordingly, we discuss an advanced numerical method that is based on this new, higher-order continuum theory. The challenges include properly incorporating the higher-order velocity gradients and stabilizing the pressure field. The flow equation arising from the second-gradient theory involves fourth-order partial derivatives. Hence, a standard Galerkin approximation requires C^1-continuous basis functions such that both the velocity field and its first derivatives are continuous. Examples include functions based on Hermite polynomials. While relatively simple to construct on uniform meshes, unstructured meshes present difficulties and certain partitions are not permissible with isoparametric versions of Hermite elements; cf., e.g. Petera and Pittman [7]. Further, additional care is required to impose boundary conditions for a theory stemming from a (classically) second-order problem using elements designed for fourth-order problems. Mixed finite-element methods present a relatively expensive alternative, requiring separate approximations for primary and secondary fields; cf., e.g. Fortin and Brezzi [8].

To overcome some of the drawbacks of these traditional methods, we adapt the continuous/discontinuous Galerkin (CDG) method proposed by Engel et al. [9]. This is essentially a non-conforming method—as the basis functions, while continuous, do not lie in the proper space for a strict Galerkin method. Continuity requirements for the derivatives are weakly satisfied by borrowing concepts from discontinuous Galerkin methods, in particular by extending the variational equation to include stabilization terms on interelement boundaries. Engel et al. [9] successfully applied the method to solve problems involving fourth-order elliptic operators arising from theories for thin beams and plates and strain gradient elasticity. Here, we develop a comparable formulation for a gradient theory for the flow of incompressible fluids.

The CDG method we employ here builds upon important concepts from the discontinuous Galerkin (DG) literature, in particular those schemes designed for spatial (as opposed to temporal) discontinuities. Much of this work is associated with problems in fluid mechanics. Bassi and Rebay [14] proposed a DG method for solving the Euler equations, which led to subsequent developments for the Navier–Stokes equations. Their method was generalized by Cockburn and Shu [17] for non-linear hyperbolic conservation laws, and later analyzed by Brezzi et al. [15]. Additional work concerns the *hp*-adaptive DG method of Bey and Oden [16] for first order problems. We refer the interested reader to the review provided in Engel et al. [9] for additional background.

The aforementioned DG methods approached second-order problems by rewriting the equations as a system of coupled, first-order equations. The work we present in this paper is more closely tied to an alternative approach introduced for elliptic and parabolic problems by Nitsche [11]. A similar effort to consistently embed constraints into a weak form was proposed by Babuška [12]. Dupont and Dupont [13] subsequently built upon Nitsche's method to develop interior penalty methods for linear second-order elliptic and parabolic equations. Baumann's [18] work on a discontinuous finite element method for fluid mechanics also relies on concepts that can be traced back to the work of Nitsche.

The outline of this paper is as follows. In the next section, we introduce general balance equations and the boundary conditions developed by Fried and Gurtin [5]. Section 3 describes the weak formulation for the newly developed flow equations. In Section 4, we introduce the non-conforming variational formulation and discretization with finite elements for the second-gradient theory. Numerical examples investigating the performance of the method are provided in Section 5. Finally a summary and concluding remarks are given in Section 6.

2. Governing equations

We work with the generalized equations for fluid flow introduced by Fried and Gurtin [5]. The theory is based on a non-standard form of the principle of virtual power provided by Gurtin [1]. The principle of virtual power is used as a basic tool in determining the structure of the tractions and of the local force balances. Classically, the power expended within an arbitrary control volume R in the region of space occupied by the deformed body has the simple form

$$\mathscr{W}_{\text{int}}(R) = \int_R \mathbf{T} : \operatorname{grad}\mathbf{v}\,\mathrm{d}v = \int_R T_{ij} v_{i,j}\,\mathrm{d}v \tag{1}$$

with $\mathbf{T}$ the Cauchy stress and $\mathbf{T}$:grad $\mathbf{v}$ the stress power. Fried and Gurtin [5] (see also Fried and Gurtin [4]) generalize the classical theory by including, in the internal power, a term linear in the gradient grad $\boldsymbol{\omega}$ of the vorticity $\boldsymbol{\omega} = \operatorname{curl}\mathbf{v}$. Specifically, a second-order tensor-valued *hyperstress* $\mathbf{G}$ is introduced via an internal power expenditure of the form $\mathbf{G}$:grad $\boldsymbol{\omega}$. The internal power expended within R then becomes

$$\mathscr{W}_{\text{int}}(R) = \int_R (\mathbf{T} : \operatorname{grad}\mathbf{v} + \mathbf{G} : \operatorname{grad}\boldsymbol{\omega})\,\mathrm{d}v = \int_R (T_{ij} v_{i,j} + G_{ij}\omega_{i,j})\,\mathrm{d}v. \tag{2}$$

In conjunction with the internal power expenditure (2), Fried and Gurtin [5] introduce a corresponding external power expenditure

$$\mathscr{W}_{\text{ext}}(R) = \int_{\mathscr{S}} \left(\mathbf{t}_{\mathscr{S}} \cdot \mathbf{v} + \mathbf{m}_{\mathscr{S}} \cdot \frac{\partial \mathbf{v}}{\partial n}\right) \mathrm{d}a + \int_R \mathbf{b} \cdot \mathbf{v}\,\mathrm{d}v \tag{3}$$

in which $\mathbf{t}_{\mathscr{S}}$ and $\mathbf{m}_{\mathscr{S}}$ represent tractions on the bounding surface $\mathscr{S} = \partial R$ of R, while $\mathbf{b}$ *represents the net inertial and non-inertial body force* acting within the body. Here the term

$$\mathbf{m}_{\mathscr{S}} \cdot \frac{\partial \mathbf{v}}{\partial n},$$

which is not present in classical theories, is needed to balance the effects of the internal-power term $\mathbf{G}$:grad $\boldsymbol{\omega}$, which involves the second gradient of $\mathbf{v}$.

The principle of virtual power replaces $\mathbf{v}$ by $\tilde{\mathbf{v}}$ and $\boldsymbol{\omega}$ by curl $\tilde{\mathbf{v}}$ and is based on the requirement that

$$\mathscr{W}_{\text{ext}}(R, \tilde{\mathbf{v}}) = \mathscr{W}_{\text{int}}(R, \tilde{\mathbf{v}}) \tag{4}$$

for all control volumes R and any choice of the virtual velocity field $\tilde{\mathbf{v}}$. Consequences of the virtual power principle and the requirement that the internal power expenditure be frame-indifferent are that:

(i) The classical macroscopic balance $\rho\dot{\mathbf{v}} = \operatorname{div}\mathbf{T}$ must be replaced by the balance

$$\rho\dot{\mathbf{v}} = \operatorname{div}\mathbf{T} + \operatorname{curl}\operatorname{div}\mathbf{G} \tag{5}$$

with $\mathbf{T}$ symmetric as in the classical theory.

(ii) Cauchy's classical condition $\mathbf{t}_{\mathscr{S}} = \mathbf{T}\mathbf{n}$ for the traction across a surface $\mathscr{S}$ with unit normal $\mathbf{n}$ must be replaced by the conditions

$$\left.\begin{aligned} \mathbf{t}_{\mathscr{S}} &= \mathbf{T}\mathbf{n} + \operatorname{div}_{\mathscr{S}}(\mathbf{G}\mathbf{n}\times) + \mathbf{n}\times(\operatorname{div}\mathbf{G} - 2K\mathbf{G}\mathbf{n}), \\ \mathbf{m}_{\mathscr{S}} &= \mathbf{n}\times\mathbf{G}\mathbf{n} \end{aligned}\right\} \tag{6}$$

in which $\operatorname{div}_{\mathscr{S}}$ is the divergence operator on $\mathscr{S}$ and $K = -\frac{1}{2}\operatorname{div}_{\mathscr{S}}\mathbf{n}$ is the mean curvature of $\mathscr{S}$.

In (5), $\mathbf{v}$ is subject to the incompressibility constraint

$$\operatorname{div}\mathbf{v} = 0, \tag{7}$$

$\dot{\mathbf{v}} = \partial\mathbf{v}/\partial t + (\operatorname{grad}\mathbf{v})\mathbf{v}$ (often written as $\mathrm{D}\mathbf{v}/\mathrm{D}t$) is the material time derivative of $\mathbf{v}$, p is the pressure, and Δ is the Laplace operator. In $(6)_2$, $\mathbf{w}\times$ denotes the axial tensor of a vector $\mathbf{w}$, as defined via the requirement that

$$(\mathbf{w}\times)\mathbf{u} = \mathbf{w}\times\mathbf{u}$$

for all vectors $\mathbf{u}$; alternatively, given an orthonormal Cartesian basis $\{\mathbf{e}_1, \mathbf{e}_2, \mathbf{e}_3\}$ and using ϵ_{ijk} to denote the alternating symbol,

$$(\mathbf{w}\times)_{ij} = \mathbf{e}_i \cdot [(\mathbf{w}\times)\mathbf{e}_j] = \epsilon_{ikj} w_k.$$

When supplemented by constitutive equations for the stress and hyperstress, the balance (5) yields a flow equation. Consistent with (7), we restrict attention to incompressible fluids and invoke the standard decomposition

$$\mathbf{T} = \mathbf{S} - p\mathbf{1}, \quad \operatorname{tr}\mathbf{S} = 0 \tag{8}$$

of the stress into a traceless extra stress $\mathbf{S}$ and a powerless pressure p. Further, we take the extra stress to be of the form

$$\mathbf{S} = 2\mu\mathbf{D}, \quad \mu > 0, \tag{9}$$

where $\mathbf{D} = \frac{1}{2}(\operatorname{grad}\mathbf{v} + (\operatorname{grad}\mathbf{v})^{\top})$ is the stretch-rate.[1] Further, we take the hyperstress to be of the simple linear form

$$\mathbf{G} = \mu L^2(\operatorname{grad}\boldsymbol{\omega} + \iota(\operatorname{grad}\boldsymbol{\omega})^{\top}) \tag{10}$$

with $-1 \leqslant \iota \leqslant 1$ to ensure non-negative dissipation. Without loss of generality, we take $L > 0$. Following Fried and Gurtin [4], we refer to L as the gradient length.

Using (8)–(10) in (5) and assuming that μ, L, and ι are constant, we arrive at the flow equation

$$\rho\dot{\mathbf{v}} = -\operatorname{grad} p + \mu\Delta(\mathbf{v} - L^2\Delta\mathbf{v}), \tag{11}$$

which, in Cartesian components, has the equivalent form $\rho\dot{v}_i = -p_{,i} + \mu(v_i - L^2 v_{i,kk})_{,jj}$.

In addition to the flow equation, the theory also provides boundary conditions. In particular, the classical no-slip boundary boundary condition is replaced by the generalized adherence conditions

$$\mathbf{v} = \mathbf{0} \quad \text{and} \quad \mathbf{m}_{\mathscr{S}} = -\mu l\boldsymbol{\omega}\times\mathbf{n} \tag{12}$$

in which the constitutive modulus $l \geqslant 0$, the adherence length, measures the strength of the fluid's adherence to the boundary. Alternatively, the theory provides conditions at solid boundaries with slip and conditions at free surfaces, each of which involves the introduction of an additional constitutive parameter. While it does not enter the flow equation (11), the parameter ι may, in general, enter the boundary condition $(12)_2$.

Whereas the quantities μL^2 and μl admit obvious interpretations as a hyperviscosity and a boundary viscosity, respectively, the parameter ι is a measure of the asymmetry of the hyperstress. Effects associated with any asymmetry of the hyperstress can therefore be felt only at the boundary of the flow domain. See Fried and Gurtin [4,5] for a comprehensive justification and discussion of the constitutive equations (9) and (10) and the boundary conditions (12).

Within the context of the kinetic theory, the Knudsen number Kn is defined as the ratio of the mean free path to a representative length scale for the flow domain. Conventionally, Navier–Stokes theory is thought to provide a physically faithful description of flow phenomena only for sufficiently small values of Kn. If we use ℓ to denote a representative length scale for the flow domain, we might therefore expect that the ratios L/ℓ and l/ℓ determined by the gradient and adherence lengths would be of $O(Kn)$. Only in problems where these ratios are sufficiently large would the additional terms appearing in the flow equation (11) and the boundary condition $(12)_2$ be of importance.

[1] To encompass the NS-α model, Fried and Gurtin [5] include a term proportional to the corotational rate of $\mathbf{D}$ in the extra stress. That term is neglected here.

3. Variational formulation

Because the general flow equation (5) and boundary conditions (6) follow from the application of the principle of virtual power, it is fairly straightforward to derive a variational formulation of the flow equation and the boundary conditions (12). Here rather than using an arbitrary control volume R, we work with the region B occupied by the body at a fixed time t.

We consider *boundary conditions* in which a portion $\mathscr{S}_{\text{free}}$ of ∂B is free and the remainder $\mathscr{S}_{\text{fxd}}$ is fixed:

$$\left.\begin{array}{l} \left.\begin{array}{l} \mathbf{T}\mathbf{n} + \operatorname{div}_{\mathscr{S}}(\mathbf{G}\mathbf{n}\times) + \mathbf{n}\times\operatorname{div}\mathbf{G} = \sigma K\mathbf{n} \\ \text{and} \quad \mathbf{n}\times\mathbf{G}\mathbf{n} = \mathbf{0} \end{array}\right\} \quad \text{on } \mathscr{S}_{\text{free}}, \\ \mathbf{v} = \mathbf{0} \quad \text{and} \quad \mathbf{n}\times\mathbf{G}\mathbf{n} = -\mu l\boldsymbol{\omega}\times\mathbf{n} \quad \text{on } \mathscr{S}_{\text{fxd}}; \end{array}\right\} \tag{13}$$

cf. (12). Here, σ denotes the surface tension.

We refer to an arbitrary virtual velocity field $\tilde{\mathbf{v}}$ as *kinematically admissible* if

$$\tilde{\mathbf{v}} = \mathbf{0} \quad \text{on } \mathscr{S}_{\text{fxd}}. \tag{14}$$

Given such a field, we consider the virtual-power balance (4) applied with $R = B$, neglecting (non-inertial) body forces, and with the replacements indicated by

$$\mathbf{t}_{\mathscr{S}} \to \sigma K\mathbf{n} \quad \text{and} \quad \mathbf{m}_{\mathscr{S}} \to \mathbf{0} \text{ on } \mathscr{S}_{\text{free}}, \qquad \mathbf{m}_{\mathscr{S}} \to -\mu l\boldsymbol{\omega}\times\mathbf{n} \text{ on } \mathscr{S}_{\text{fxd}}. \tag{15}$$

We write $\mathscr{V}$ and $\mathscr{P}$ for the spaces of admissible velocity and pressure fields, respectively. The two-field variational form reads: find $(\mathbf{v}, p) \in \mathscr{V}\times\mathscr{P}$ such that

$$T(\mathbf{v}, p, \tilde{\mathbf{v}}, \tilde{p}) = \ell(\tilde{\mathbf{v}}) \tag{16}$$

for all $(\tilde{\mathbf{v}}, \tilde{p}) \in \mathscr{V}\times\mathscr{P}$, where

$$\begin{aligned} T(\mathbf{v}, p, \tilde{\mathbf{v}}, \tilde{p}) = {} & \int_B (\mathbf{S} : \operatorname{grad}\tilde{\mathbf{v}} + \mathbf{G} : \operatorname{grad}\operatorname{curl}\tilde{\mathbf{v}})\,\mathrm{d}v + \int_{\mathscr{S}_{\text{fxd}}} (\mu l\boldsymbol{\omega}\times\mathbf{n})\cdot\frac{\partial\tilde{\mathbf{v}}}{\partial n}\,\mathrm{d}a - \int_B p\operatorname{div}\tilde{\mathbf{v}}\,\mathrm{d}v \\ & - \int_B \tilde{p}\operatorname{div}\mathbf{v}\,\mathrm{d}v - \int_B \rho\dot{\mathbf{v}}\cdot\tilde{\mathbf{v}}\,\mathrm{d}v \end{aligned} \tag{17}$$

and

$$\ell(\tilde{\mathbf{v}}) = \int_{\mathscr{S}_{\text{free}}} \sigma K\mathbf{n}\cdot\tilde{\mathbf{v}}\,\mathrm{d}a. \tag{18}$$

To obtain correspondence with the particular flow equation (11), $\mathbf{S}$ and $\mathbf{G}$ are given by (9) and (10), respectively.

4. Discretization of the second gradient theory

In this section, we introduce our numerical formulation for the second-gradient theory. Our work is based on the non-conforming method proposed by Engel et al. [9]. In this approach, the basis functions are C^0-continuous—so that their first and higher-order derivatives are discontinuous. Continuity of the first and higher-order derivatives is weakly enforced by adding weighted residual terms to the variational equation on element boundaries and invoking stabilization techniques. The number of unknowns per element arising for this method is considerably fewer than for alternatives based on traditional strategies such as C^1-continuous basis functions.

The spaces of admissible velocity and pressure fields are $\mathscr{V} \subset H^2(B)$ and $\mathscr{P} \subset H^0(B)$, where $H^m(B)$ denotes the classical Sobolev space of order m. We use a non-conforming Galerkin method to approximate the solution to (16), and we state the weak form of the variational problem in terms of finite-dimensional spaces $\mathscr{V}^h \subset H^1(B)$ and $\mathscr{P}^h \subset \mathscr{P}$.

To construct the bases, we consider a regular finite-element partition $\mathscr{Q}^h = \cup_{e=1}^{M}\mathscr{Q}_e$, with $\mathscr{Q}^h \approx B$ and M the total number of elements in the mesh. We choose approximation functions which are continuous on the entire domain but discontinuous in first and higher-order derivatives across element boundaries. Further, we consider element interiors $\widetilde{\mathscr{Q}}$ defined via

$$\widetilde{\mathcal{Q}} = \bigcup_{e=1}^{M} \mathcal{Q}_e. \tag{19}$$

The union $\widetilde{\Gamma}$ of interior boundaries is expressed as

$$\widetilde{\Gamma} = \bigcup_{i=1}^{N_i} \Gamma_i, \tag{20}$$

where N_i denotes the number of element *interior* boundaries. In two dimensions, these refer only to those element edges that are shared by two spatially adjacent elements, and do not include edges along the physical boundary ∂B. Given a field f on B, the jump $[\![f]\!]$ of f across the interior boundary is defined as

$$[\![f]\!] = f^+ - f^-, \tag{21}$$

where

$$f^{\pm} = \lim_{\epsilon \to 0} f(\mathbf{x} \mp \epsilon \mathbf{n}) \tag{22}$$

and $\mathbf{n}$ is any of the two unit normals to the interior boundary and $\epsilon > 0$. The jump operator is graphically described in Fig. 1. The average $\langle\!\langle f \rangle\!\rangle$ of f across the interior boundary is defined as

$$\langle\!\langle f \rangle\!\rangle = \frac{1}{2}(f^+ + f^-). \tag{23}$$

From the definitions of the jump and average operators, we have the useful identity

$$[\![fg]\!] = [\![f]\!]\langle\!\langle g \rangle\!\rangle + \langle\!\langle f \rangle\!\rangle [\![g]\!]. \tag{24}$$

The method we propose to approximate the solution to flow problems arising from the second-gradient theory can then be stated as: find $(\mathbf{v}^h, p^h) \in \mathscr{V}^h \times \mathscr{P}^h$ such that

$$T_{cd}(\mathbf{v}^h, p^h, \tilde{\mathbf{v}}^h, \tilde{p}^h) = \ell_{cd}(\tilde{\mathbf{v}}^h), \quad \forall (\tilde{\mathbf{v}}^h, \tilde{p}^h) \in \mathscr{V}^h \times \mathscr{P}^h, \tag{25}$$

where the bilinear form T_{cd} is defined via

$$\begin{aligned} T_{cd}(\mathbf{v}^h, p^h, \tilde{\mathbf{v}}^h, \tilde{p}^h) = & \int_{\widetilde{\mathcal{Q}}} (\mathbf{S}^h : \operatorname{grad} \tilde{\mathbf{v}}^h + \mathbf{G}^h : \operatorname{grad} \operatorname{curl} \tilde{\mathbf{v}}^h)\, \mathrm{d}v - \int_{\widetilde{\Gamma}} \langle\!\langle \widetilde{\mathbf{G}}^h \mathbf{n} \rangle\!\rangle \cdot [\![\operatorname{curl} \mathbf{v}^h]\!]\, \mathrm{d}a \\ & - \int_{\widetilde{\Gamma}} [\![\operatorname{curl} \tilde{\mathbf{v}}^h]\!] \cdot \langle\!\langle \mathbf{G}^h \mathbf{n} \rangle\!\rangle\, \mathrm{d}a + \tau_v \int_{\widetilde{\Gamma}} [\![\operatorname{curl} \tilde{\mathbf{v}}^h]\!] \cdot [\![\operatorname{curl} \mathbf{v}^h]\!]\, \mathrm{d}a - \int_{\widetilde{\mathcal{Q}}} p^h \operatorname{div} \tilde{\mathbf{v}}^h\, \mathrm{d}v \\ & - \int_{\widetilde{\mathcal{Q}}} \tilde{p}^h \operatorname{div} \mathbf{v}^h \mathrm{d}v - \int_{\widetilde{\mathcal{Q}}} \rho \dot{\mathbf{v}}^h \cdot \tilde{\mathbf{v}}^h\, \mathrm{d}v + \int_{\mathscr{S}_{\mathrm{fxd}}} (\mu l \boldsymbol{\omega} \times \mathbf{n}) \cdot \frac{\partial \tilde{\mathbf{v}}^h}{\partial n}\, \mathrm{d}a \end{aligned} \tag{26}$$

and the linear form ℓ_{cd} is defined via

$$\ell_{cd}(\tilde{\mathbf{v}}^h) = \int_{\mathscr{S}_{\mathrm{free}}} \sigma K \mathbf{n} \cdot \tilde{\mathbf{v}}^h\, \mathrm{d}a. \tag{27}$$

In (26), τ_v denotes the velocity stabilization parameter for the interelement boundaries. The basic structure of this stabilized approach follows from Nitsche's method [11] for enforcing constraints on interfaces.

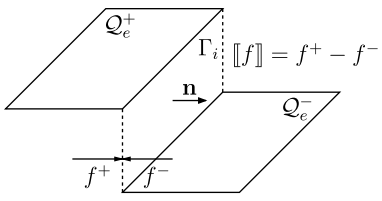

Fig. 1. Graphical description of jump operator.

We remark that the imposition of generalized adherence boundary conditions on fixed surfaces does not require a priori knowledge of the vorticity field on those surfaces. The generalized boundary conditions are enforced as a Robin-type, and we need only to express the vorticity in terms of the approximation to the velocity field, i.e.

$$\boldsymbol{\omega} = \operatorname{curl} \mathbf{v}^h. \tag{28}$$

From dimensional arguments, we can infer that the parameter τ_v should be $C_v \mu L^2/h_e$ where h_e is the characteristic size of the element edge, and C_v is a proportionality constant. Such a scaling with mesh spacing is likely the minimum requirement to maintain convergence, and is consistent with error estimates provided in Engel et al. [9]. We expect the optimal proportionality constant to be a function of the particular choices of bases for the velocity and pressure fields. While the proportionality constant can be determined analytically in some cases, at present there does not exist a general approach. In Section 5, we explore a strategy based on solutions to benchmark problems.

Many of the jump terms appearing in (26) stem from the divergence theorem as applied to volume integrals over individual elements (see the following proof of consistency). In particular, surface integrals involving normal flux quantities (such as $\mathbf{T}\mathbf{n}_e$ or $\mathbf{G}\mathbf{n}_e$) arise over the boundary of each element $\mathscr{Q}_e$, where $\mathbf{n}_e$ denotes the unit outward normal to $\mathscr{Q}_e$. Since adjacent elements possess equal and opposite normal vectors along common interior boundaries, the choice of positive normal (and thus positive side) is arbitrary for any given pair. However, the particular choice of normal for any given edge does not affect the final result, as the normal always appears in the conjugate term in all inner-product forms in (26). For consistency, it is important that once a positive side is identified on a given element interior, it is identified as such for each of the jump terms appearing in (26).

4.1. Consistency

The consistency of the method is derived through successive application of the divergence theorem to (25). Using the equality (24), we derive

$$\begin{aligned}\int_{\widetilde{\mathscr{Q}}} \mathbf{T}^h : \operatorname{grad} \tilde{\mathbf{v}}^h \,\mathrm{d}v &= -\int_{\widetilde{\mathscr{Q}}} \operatorname{div} \mathbf{T}^h \cdot \tilde{\mathbf{v}}^h \,\mathrm{d}v + \int_{\mathscr{S}} \mathbf{T}^h \mathbf{n} \cdot \tilde{\mathbf{v}}^h \,\mathrm{d}a + \int_{\widetilde{\Gamma}} [\![\mathbf{T}^h \mathbf{n} \cdot \tilde{\mathbf{v}}^h]\!] \,\mathrm{d}a \\ &= -\int_{\widetilde{\mathscr{Q}}} \operatorname{div} \mathbf{T}^h \cdot \tilde{\mathbf{v}}^h \,\mathrm{d}v + \int_{\mathscr{S}} \mathbf{T}^h \mathbf{n} \cdot \tilde{\mathbf{v}}^h \,\mathrm{d}a + \int_{\widetilde{\Gamma}} ([\![\mathbf{T}^h \mathbf{n}]\!] \cdot \langle\!\langle \tilde{\mathbf{v}}^h \rangle\!\rangle + \langle\!\langle \mathbf{T}^h \mathbf{n} \rangle\!\rangle \cdot [\![\tilde{\mathbf{v}}^h]\!]) \,\mathrm{d}a.\end{aligned}$$

Similarly, the divergence theorem applied twice yields

$$\begin{aligned}\int_{\widetilde{\mathscr{Q}}} \mathbf{G}^h : \operatorname{grad} \operatorname{curl} \tilde{\mathbf{v}}^h \,\mathrm{d}v &= -\int_{\widetilde{\mathscr{Q}}} (\operatorname{div} \mathbf{G}^h) \cdot (\operatorname{curl} \tilde{\mathbf{v}}^h) \,\mathrm{d}v + \int_{\mathscr{S}} \mathbf{G}^h \mathbf{n} \cdot \operatorname{curl} \tilde{\mathbf{v}}^h \,\mathrm{d}a + \int_{\widetilde{\Gamma}} [\![\mathbf{G}^h \mathbf{n} \cdot \operatorname{curl} \tilde{\mathbf{v}}^h]\!] \,\mathrm{d}a \\ &= -\int_{\widetilde{\mathscr{Q}}} (\operatorname{curl} \operatorname{div} \mathbf{G}^h) \cdot \tilde{\mathbf{v}}^h \,\mathrm{d}v + \int_{\mathscr{S}} (\mathbf{G}^h \mathbf{n} \cdot \operatorname{curl} \tilde{\mathbf{v}}^h + (\mathbf{n} \times \operatorname{div} \mathbf{G}^h) \cdot \tilde{\mathbf{v}}^h) \,\mathrm{d}a \\ &\quad + \int_{\widetilde{\Gamma}} ([\![\mathbf{G}^h \mathbf{n} \cdot \operatorname{curl} \tilde{\mathbf{v}}^h]\!] + [\![(\mathbf{n} \times \operatorname{div} \mathbf{G}^h) \cdot \tilde{\mathbf{v}}^h]\!]) \,\mathrm{d}a \\ &= -\int_{\widetilde{\mathscr{Q}}} (\operatorname{curl} \operatorname{div} \mathbf{G}^h) \cdot \tilde{\mathbf{v}}^h \,\mathrm{d}v + \int_{\mathscr{S}} (\mathbf{G}^h \mathbf{n} \cdot \operatorname{curl} \tilde{\mathbf{v}}^h + (\mathbf{n} \times \operatorname{div} \mathbf{G}^h) \cdot \tilde{\mathbf{v}}^h) \,\mathrm{d}a \\ &\quad + \int_{\widetilde{\Gamma}} ([\![\mathbf{G}^h \mathbf{n}]\!] \cdot \langle\!\langle \operatorname{curl} \tilde{\mathbf{v}}^h \rangle\!\rangle + \langle\!\langle \mathbf{G}^h \mathbf{n} \rangle\!\rangle \cdot [\![\operatorname{curl} \tilde{\mathbf{v}}^h]\!]) \,\mathrm{d}a + \int_{\widetilde{\Gamma}} ([\![\mathbf{n} \times \operatorname{div} \mathbf{G}^h]\!] \cdot \langle\!\langle \tilde{\mathbf{v}}^h \rangle\!\rangle \\ &\quad + \langle\!\langle (\mathbf{n} \times \operatorname{div} \mathbf{G}^h) \rangle\!\rangle \cdot [\![\tilde{\mathbf{v}}^h]\!]) \,\mathrm{d}a.\end{aligned}$$

Since $\tilde{\mathbf{v}}^h$ is continuous on the interelement boundary $\widetilde{\Gamma}$, we have $[\![\tilde{\mathbf{v}}^h]\!] = \mathbf{0}$, yielding

$$\int_{\widetilde{\mathscr{Q}}} \mathbf{T}^h : \operatorname{grad} \tilde{\mathbf{v}}^h \,\mathrm{d}v = -\int_{\widetilde{\mathscr{Q}}} \operatorname{div} \mathbf{T}^h \cdot \tilde{\mathbf{v}}^h \,\mathrm{d}v + \int_{\mathscr{S}} \mathbf{T}^h \mathbf{n} \cdot \tilde{\mathbf{v}}^h \,\mathrm{d}a + \int_{\widetilde{\Gamma}} [\![\mathbf{T}^h \mathbf{n}]\!] \cdot \langle\!\langle \tilde{\mathbf{v}}^h \rangle\!\rangle \,\mathrm{d}a \tag{29}$$

and

$$\int_{\widetilde{\mathscr{D}}} \mathbf{G}^h : \operatorname{grad}\operatorname{curl}\tilde{\mathbf{v}}^h \,\mathrm{d}v = -\int_{\widetilde{\mathscr{D}}} (\operatorname{curl}\operatorname{div}\mathbf{G}^h)\cdot\tilde{\mathbf{v}}^h \,\mathrm{d}v + \int_{\mathscr{S}} (\mathbf{G}^h\mathbf{n}\cdot\operatorname{curl}\tilde{\mathbf{v}}^h + (\mathbf{n}\times\operatorname{div}\mathbf{G}^h)\cdot\tilde{\mathbf{v}}^h)\,\mathrm{d}a + \int_{\widetilde{\Gamma}} (\llbracket \mathbf{G}^h\mathbf{n}\rrbracket\cdot\langle\!\langle \operatorname{curl}\tilde{\mathbf{v}}^h\rangle\!\rangle + \langle\!\langle \mathbf{G}^h\mathbf{n}\rangle\!\rangle\cdot\llbracket\operatorname{curl}\tilde{\mathbf{v}}^h\rrbracket)\,\mathrm{d}a + \int_{\widetilde{\Gamma}} \llbracket \mathbf{n}\times\operatorname{div}\mathbf{G}^h\rrbracket\cdot\langle\!\langle\tilde{\mathbf{v}}^h\rangle\!\rangle\,\mathrm{d}a. \tag{30}$$

Here, we take advantage of the equality

$$\int_{\mathscr{S}} \mathbf{G}^h\mathbf{n}\cdot\operatorname{curl}\tilde{\mathbf{v}}^h \mathrm{d}a = \int_{\mathscr{S}} \left((\operatorname{div}_{\mathscr{S}}(\mathbf{G}^h\mathbf{n}\times) - 2K\mathbf{n}\times\mathbf{G}^h\mathbf{n})\cdot\tilde{\mathbf{v}}^h + (\mathbf{n}\times\mathbf{G}^h\mathbf{n})\cdot\frac{\partial\tilde{\mathbf{v}}^h}{\partial n}\right)\mathrm{d}a. \tag{31}$$

A detailed derivation of this equality is provided by Fried and Gurtin [5].

The consistency of the method then follows upon substituting the results (29)–(31), into (26), viz.

$$\begin{aligned} 0 &= T_{cd}(\mathbf{v}^h, p^h, \tilde{\mathbf{v}}^h, \tilde{p}^h) - \ell_{cd}(\tilde{\mathbf{v}}^h) \\ &= \int_{\widetilde{\mathscr{D}}} (\operatorname{curl}\operatorname{div}\mathbf{G}^h + \operatorname{div}\mathbf{T}^h - \rho\dot{\mathbf{v}}^h)\cdot\tilde{\mathbf{v}}^h \,\mathrm{d}v - \int_{\widetilde{\Gamma}} \langle\!\langle \widetilde{\mathbf{G}}^h\mathbf{n}\rangle\!\rangle\cdot\llbracket\operatorname{curl}\mathbf{v}^h\rrbracket\,\mathrm{d}a + \int_{\widetilde{\Gamma}} \llbracket \mathbf{T}^h\mathbf{n} + \mathbf{n}\times\operatorname{div}\mathbf{G}^h \\ &\quad + \operatorname{div}_{\mathscr{S}}(\mathbf{G}^h\mathbf{n}\times) - 2K\mathbf{n}\times\mathbf{G}^h\mathbf{n}\rrbracket\cdot\langle\!\langle\tilde{\mathbf{v}}^h\rangle\!\rangle\,\mathrm{d}a + \int_{\widetilde{\Gamma}} \llbracket \mathbf{n}\times\mathbf{G}^h\mathbf{n}\rrbracket\cdot\left\langle\!\!\left\langle \frac{\partial\tilde{\mathbf{v}}^h}{\partial n}\right\rangle\!\!\right\rangle \mathrm{d}a \\ &\quad + \int_{\mathscr{S}_{\text{free}}} (\mathbf{T}^h\mathbf{n} + \mathbf{n}\times\operatorname{div}\mathbf{G}^h + \operatorname{div}_{\mathscr{S}}(\mathbf{G}^h\mathbf{n}\times) - 2K\mathbf{n}\times\mathbf{G}^h\mathbf{n} - \sigma K\mathbf{n})\cdot\tilde{\mathbf{v}}^h\,\mathrm{d}a + \int_{\mathscr{S}_{\text{free}}} (\mathbf{n}\times\mathbf{G}^h\mathbf{n})\cdot\frac{\partial\tilde{\mathbf{v}}^h}{\partial n}\mathrm{d}a \\ &\quad + \int_{\mathscr{S}_{\text{fxd}}} (\mathbf{n}\times\mathbf{G}^h\mathbf{n} - \mu l\boldsymbol{\omega}\times\mathbf{n})\cdot\frac{\partial\tilde{\mathbf{v}}^h}{\partial n}\,\mathrm{d}a + \tau_v\int_{\widetilde{\Gamma}} \llbracket\operatorname{curl}\tilde{\mathbf{v}}^h\rrbracket\cdot\llbracket\operatorname{curl}\mathbf{v}^h\rrbracket\,\mathrm{d}a. \end{aligned} \tag{32}$$

From (32) we deduce the second gradient equations

$$\operatorname{div}\mathbf{T}^h + \operatorname{curl}\operatorname{div}\mathbf{G}^h = \rho\dot{\mathbf{v}}^h \quad \text{in}\,\widetilde{\mathscr{D}}, \tag{33}$$

$$\left.\begin{array}{l} \mathbf{T}^h\mathbf{n} + \mathbf{n}\times\operatorname{div}\mathbf{G}^h + \operatorname{div}_{\mathscr{S}}(\mathbf{G}^h\mathbf{n}\times) - 2K\mathbf{n}\times\mathbf{G}^h\mathbf{n} = \sigma K\mathbf{n} \\ \text{and } \mathbf{n}\times\mathbf{G}^h\mathbf{n} = \mathbf{0} \end{array}\right\} \quad \text{on } \mathscr{S}_{\text{free}}, \qquad \mathbf{n}\times\mathbf{G}^h\mathbf{n} = -\mu l\boldsymbol{\omega}\times\mathbf{n} \quad \text{on } \mathscr{S}_{\text{fxd}}, \tag{34}$$

and the jump conditions

$$\left.\begin{array}{l} \llbracket\operatorname{curl}\mathbf{v}^h\rrbracket = \mathbf{0}, \\ \llbracket \mathbf{T}^h\mathbf{n} + \mathbf{n}\times\operatorname{div}\mathbf{G}^h + \operatorname{div}_{\mathscr{S}}(\mathbf{G}^h\mathbf{n}\times) - 2K\mathbf{n}\times\mathbf{G}^h\mathbf{n}\rrbracket = \mathbf{0}, \\ \llbracket\mathbf{n}\times\mathbf{G}^h\mathbf{n}\rrbracket = \mathbf{0}, \end{array}\right\} \quad \text{on } \widetilde{\Gamma}. \tag{35}$$

While (33) enforces the flow equation on the element interiors, (34) enforces the boundary conditions on free and fixed surfaces of the flow domain, $(35)_1$ ensures the continuity of the first derivatives across the interelement boundaries, and $(35)_{2,3}$ ensure the continuity of the tractions across the interelement boundaries. On replacing $\mathbf{v}$ and p in (25) by $\mathbf{v}^h$ and p^h, we obtain the Galerkin orthogonality condition

$$T_{cd}(\mathbf{e}_v, \mathbf{e}_p, \tilde{\mathbf{v}}^h, \tilde{p}^h) = 0 \quad \forall(\tilde{\mathbf{v}}^h, \tilde{p}^h) \in \mathscr{V}^h \times \mathscr{P}^h, \tag{36}$$

where $\mathbf{e}_v = \mathbf{v}^h - \mathbf{v}$ and $\mathbf{e}_p = p^h - p$ are the errors for the velocity and pressure fields, respectively.

4.2. Element choice and additional pressure stabilization

We restrict attention to problems for which the inertial terms appearing in (26) can be neglected. Extensions to time-dependent flows and the non-linearities associated with the material derivative of the velocity field for the second gradient theory are left for a future work. We will base our formulation on one that is stable for the classical theory, namely: nine-node isoparametric quadrilateral elements with piecewise-quadratic basis

functions for the velocity field and linear (discontinuous) basis functions for the pressure field. Three-dimensional generalizations of these elements are readily available and widely used in practice.

To begin, we introduce the space

$$P^j(\mathcal{Q}_e) = \{\mathbf{v} : \mathbf{v} \text{ is a polynomial of degree } \leqslant j \text{ on } \mathcal{Q}_e\} \tag{37}$$

of complete polynomials over element $\mathcal{Q}_e$. Using N to denote the number of nodes in the mesh, we then write

$$\{\phi_I\} = \{\phi_I \in C^0(\mathcal{Q}^h) : \phi_I|\mathcal{Q}_e \in P^2(\mathcal{Q}_e)\}, \quad I = 1 \ldots N \tag{38}$$

for the set of quadratic Lagrangian isoparametric functions. The approximation to the velocity field is then given by

$$\mathbf{v}^h(\mathbf{x}) = \sum_{I=1}^{N} \phi_I(\boldsymbol{\xi}(\mathbf{x}))\mathbf{v}_I, \tag{39}$$

where $\mathbf{v}_I$ is the nodal value at node I and $\boldsymbol{\xi}$ is the position in a reference element.

For the pressure field, we introduce the set

$$\{M_I\} = \{M_I \in H^0(\mathcal{Q}^h) : M_I|\mathcal{Q}_e \in P^1(\mathcal{Q}_e)\}, \quad I = 1 \ldots M \tag{40}$$

of linear element-based (discontinuous) shape functions. The approximation to the pressure field p can then be written as

$$p^h(\mathbf{x}) = \sum_I M_I(\mathbf{x})p_I. \tag{41}$$

The approximations (39) and (41) over quadrilateral elements are stable for the classical problem of Stokes flow; cf., e.g. Hughes [10]. We therefore expect stability to also hold for sufficiently small gradient lengths L. However, for larger gradient lengths, we should not necessarily expect these elements to be stable. Accordingly, we investigate the use of additional pressure stabilization. In particular, we follow the approach of Hughes and Franca [19] and add terms of the form

$$-\sum_{e\in\widetilde{\Gamma}} \tau_p \int_e [\![p^h]\!][\![\tilde{p}^h]\!]\,\mathrm{d}a \tag{42}$$

to the non-conforming approximation (26), where τ_p is the pressure stability parameter. Similar to the velocity stability parameter τ_v, we expect this parameter to take the form $C_p\mu L^2/h_e$, where h_e is the characteristic length of the element edge, and C_p is another proportionality constant. Importantly, the addition of this term does not affect the consistency proof presented earlier; indeed, this term weakly enforces continuity of the pressure field between elements.

To approximate the weight functions $\tilde{\mathbf{v}}^h$ and $\tilde{p}^h$, we use expansions analogous to (39) and (41). Upon substituting these expressions into (26) (neglecting inertial terms) and invoking the arbitrariness of the weight functions, we obtain the linear algebraic system of equations

$$\begin{bmatrix} \mathbf{K}_c + \mathbf{K}_g & \mathbf{G}_c \\ \mathbf{G}_c^{\mathrm{T}} & \mathbf{S} \end{bmatrix} \begin{bmatrix} \mathbf{d}_v \\ \mathbf{d}_p \end{bmatrix} = \begin{bmatrix} \mathbf{f}_v \\ \mathbf{f}_p \end{bmatrix}, \tag{43}$$

which can be solved to yield $\mathbf{d}_v$ and $\mathbf{d}_p$.

5. Numerical examples

5.1. Benchmark problem: plane Poiseuille flow

We consider the problem of steady, laminar flow through an infinite, rectangular channel formed by two parallel surfaces separated by a gap h (Fig. 2). Writing

$$u = \mathbf{v} \cdot \mathbf{e}_x, \quad v = \mathbf{v} \cdot \mathbf{e}_y \tag{44}$$

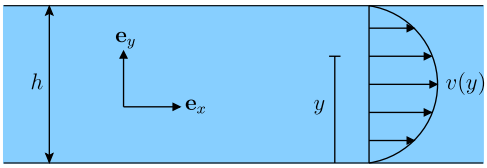

Fig. 2. Schematic of the channel for the problem of plane Poiseuille flow. The coordinates in the directions downstream and out of the plane are x and z.

for the horizontal and vertical components of the velocity field, we consider problems with solutions of the form

$$u = u(y), \quad v = 0 \tag{45}$$

as shown in Fig. 2. An analytical solution to this problem for the flow equation (11) with generalized adherency conditions (12) was developed by Fried and Gurtin [4] for a theory different from that considered here. Nevertheless, the solution to the problem of plane Poiseuille flow is identical for both theories. The pressure field is only known up to an arbitrary additive constant with gradient

$$\operatorname{grad} p = -\beta \mathbf{e}_x, \quad \text{with } \beta = \text{constant} \tag{46}$$

without loss of generality, we assume that $\beta > 0$. The solution for the velocity field can be decomposed into classical and generalized contributions as

$$u(y) = u_c(y) + u_g(y), \tag{47}$$

where

$$u_c(y) = \frac{\beta h^2}{2\mu} \frac{y}{h}\left(1 - \frac{y}{h}\right) \tag{48}$$

is the *classical solution* of the analogous problem for a Navier–Stokes fluid and

$$u_g(y) = -\frac{\beta h^2}{2\mu} \frac{b_l L}{h \sinh \frac{h}{L}}\left(\sinh \frac{h}{L} - \sinh \frac{y}{L} - \sinh \frac{h-y}{L}\right) \tag{49}$$

arises from higher-order terms characterized by the gradient length L. In view of the signs of L, l, and h, the constant

$$b_l = \frac{\frac{2L}{h} + \frac{l}{L}}{1 + \frac{l}{L} \tanh \frac{h}{2L}} \tag{50}$$

is a non-negative dimensionless measure of the effective adhesion length. The specialized conditions of weak and strong adherence arise respectively from the limits setting $l \to 0$ and $l \to \infty$.

Although the solution (49) is essentially one-dimensional in nature, we use it to establish a two-dimensional boundary value problem to verify the finite-element formulation described in Section 4. The approach we follow is to prescribe boundary conditions consistent with (49) on an arbitrary, finite "computational domain" $\mathscr{D}^h$. We then quantify the error in the numerical approximation to the velocity $\mathbf{v}$ and pressure p fields on the interior of the domain using suitable error norms. This procedure requires a priori knowledge of the solution and is only used for verifying the numerical formulation. More general boundary conditions will be discussed subsequently.

We take advantage of the symmetry of the solution (49) about the midplane of the channel and consider a numerical domain with dimensions $[0, h/2] \times [h/2, h]$ as shown in Fig. 3. On the midplane of the channel, the velocity field is constrained to be symmetric and a zero hypertraction is enforced. The top surface of the channel is considered fixed and we prescribe the generalized adherence conditions (12). It bears emphasis that while the vertical component of the velocity field is fixed to vanish on all of the boundaries of the computational domain, it is not constrained on the interior of the domain.

What remains is to designate boundary conditions on the vertical computational surfaces. Here, we choose to prescribe the velocity field only at the left (inlet) boundary according to the exact solution (49). Zero hypertractions are prescribed at the inlet and outlet.

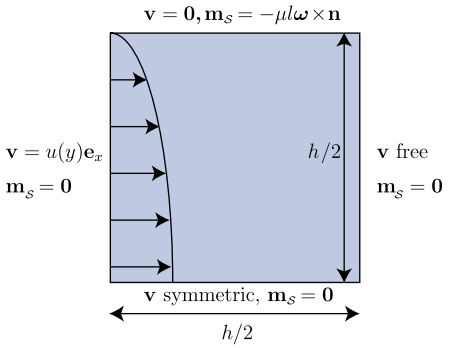

Fig. 3. Computational domain and boundary conditions for the channel flow studies.

To check convergence in the velocity field, we use the L_2-norm of the error $\mathbf{e}_v = \mathbf{v}^h - \mathbf{v}$. Since the pressure field is known only up to a constant, the appropriate norm to check convergence is the L_2-norm of the error $\mathbf{e}_p = \operatorname{grad} p^h - \operatorname{grad} p$ in the gradient of the pressure field. In the following, we report error norms that are normalized by those of the solution.

We begin by examining the limiting case of $l \to 0$, corresponding to weak adherence conditions on the channel walls. We set the gradient length L equal to $h/4$. Fig. 4 provides convergence results obtained using a sequence of uniform meshes with equidistant nodal spacing $\mathrm{d}y = \mathrm{d}x$ in each of the coordinate directions. We observe a rate of convergence in the L_2-error norm of the velocity field that lies between quadratic and cubic. For a discretization of a classical Navier–Stokes problem using the isoparametric quadratic shape functions, a cubic rate is optimal; cf. Hughes et al. [20]. In this case, the sub-optimal rate of convergence in the velocity field is likely associated with a sub-optimal choice for the stability parameter. Engel et al. [9] reported similar observations with the CDG method.

Fig. 5 juxtaposes the solution (49) and the finite-element approximation $\mathbf{v}^h$ obtained using a 4×4 uniform mesh. The latter is shown above the midplane $y/h = 0.5$ and the numerical approximation is seen to be indistinguishable from the solution.

For the pressure field, we obtain nearly a quadratic rate of convergence in the L_2 norm of $\mathbf{e}_p$ (essentially, the H^1 semi-norm of the pressure field). We are not aware of any studies detailing the accuracy of the pressure approximation for the mixed formulation described herein. However, this rate is better than expected based on the best approximation error for a linear field.

Fig. 6 compares numerical and exact solutions for the case of generalized adherence conditions ($l > 0$) on the channel wall, using various ratios l/L of adherence length to gradient length. The numerical results were

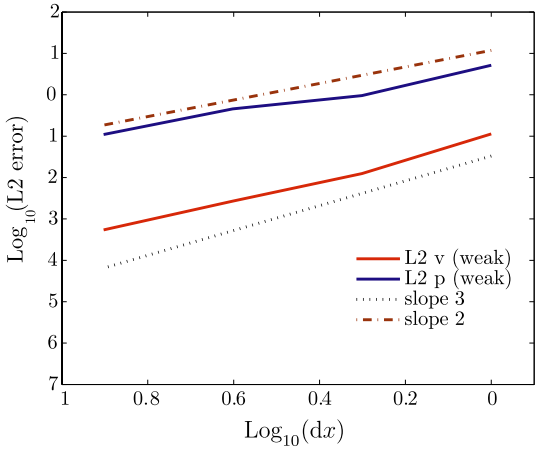

Fig. 4. Convergence results for the benchmark problem for weak adherence boundary conditions.

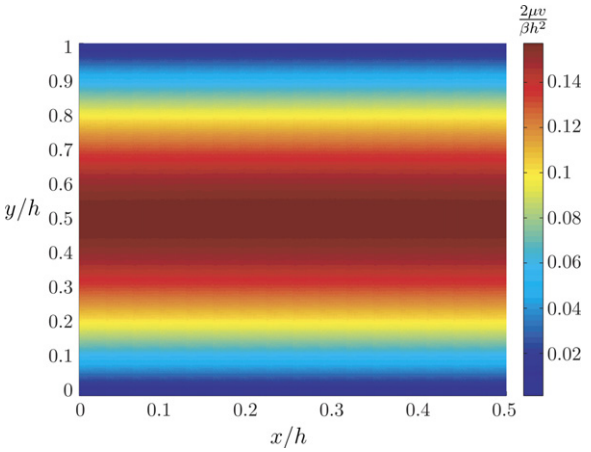

Fig. 5. Contour plot of velocity field normalized by $\beta h^2/2\mu$ for weak adherence boundary conditions. The finite-element approximation is shown above the channel center $y/h = 0.5$ and the solution (49) is shown below this line.

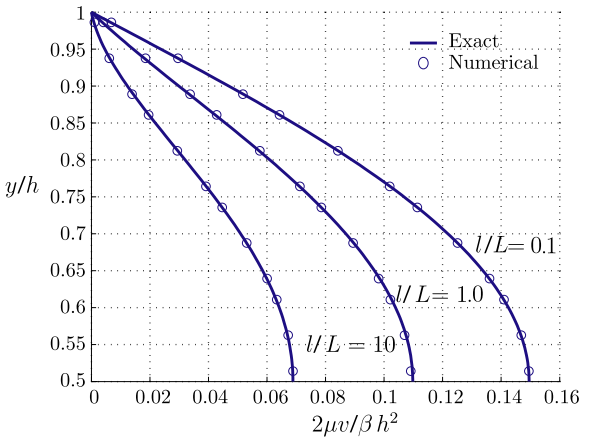

Fig. 6. Exact and numerical velocity profiles at the outlet boundary of the computational domain for various ratios l/L of adherence length to gradient length. All numerical results were obtained on a 4×4 uniform mesh.

obtained at the outflow ($x/h = 0.5$) boundary of the computational domain. All of the numerical results shown in Fig. 6 are for a uniform mesh of 4×4 elements. The results indicate an excellent match between the numerical and exact velocity fields, particularly given the coarseness of the mesh. Fig. 7 shows the contours of the normalized pressure gradient obtained for the particular choice of $l/L = 0.1$. As expected, the pressure gradient is almost constant and the maximum error is less than 3%.

A convergence study with generalized adherence boundary conditions on the channel walls yields results that are qualitatively similar to those arising for weak adherence boundary conditions. Fig. 8 compares the relative error norms for the two cases. The generalized adherence results were obtained using $l/L = 0.1$. We report that the rates of convergence are nearly unaffected with generalized adherence boundary conditions, and a slight increase in accuracy was observed with increasing mesh refinement.

As a final verification test, we report results using skewed meshes. Fig. 9 shows velocity contours for the case of generalized adherence boundary conditions with the skewed mesh geometry superimposed over the finite-element approximation to $\mathbf{v}$. The numerical results once again compare favorably to the solution.

We note that this benchmark problem also permits us to examine other choices for boundary conditions and their effect on the numerical solution. Heywood et al. [21] proposed a simple method to prescribe a pressure drop between artificial inlet and outlet boundaries such as the left and right boundaries in Fig. 3. Writing

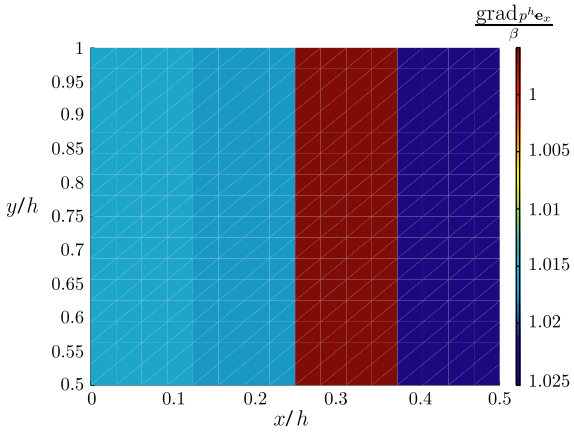

Fig. 7. Contour plot of the normalized pressure gradient $\mathbf{e}_x \cdot \text{grad}\, p^h/\beta$ for channel flow with generalized adherence boundary conditions ($l/L = 1.0$).

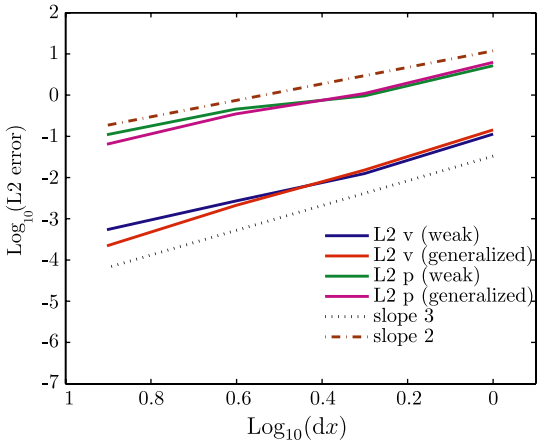

Fig. 8. Convergence results for the benchmark problem for weak and generalized adherence boundary conditions.

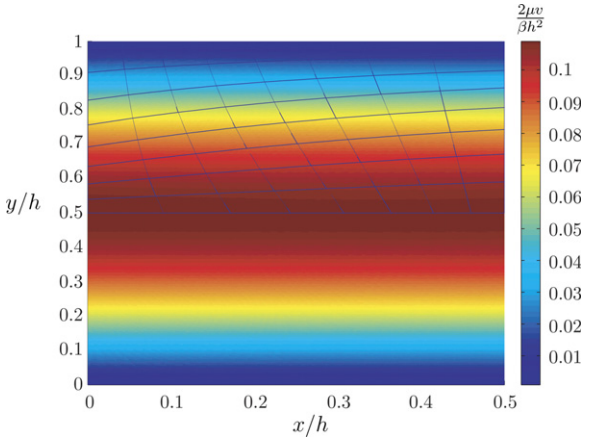

Fig. 9. Contour plot of velocity field normalized by $\beta h^2/2\mu$ for generalized adherence boundary conditions, with $l/L = 1.0$. The finite-element approximation and smoothed mesh is shown above the channel center $y/h = 0.5$ and the solution (49) is shown below this line.

$-P$ for the desired pressure drop between the artificial inlet and outlet boundaries, the approach amounts to replacing the prescribed velocity boundary condition at the inlet with a traction

$$\mathbf{t} = -P\mathbf{e}_x. \tag{51}$$

Using such an approach, we obtain nearly identical results to those obtained using the boundary conditions described in Fig. 2. This approach will be used in Section 5.3 to study flow through a channel with a step.

In the above studies, the accuracy and rate of convergence in the velocity and pressure fields were found to be sensitive to the particular choice of the proportionality constants C_v and C_p for the stability terms τ_v and τ_p, respectively. Without pressure stabilization, for example, the pressure field does not converge in some cases and the rate of convergence in the velocity field typically decreases from those reported above. While we have not conducted an exhaustive parametric study, we have found the most consistent results to be obtained using $C_v = 14$ and $C_p = 0.2$. We suggest that such a convergence study with a benchmark problem provides a mechanism to find stability parameters that are applicable to other problems with the same choice of material parameters. Indeed, the results presented in the following sections were obtained with this approach. However, better results could likely be obtained by using stabilization parameters that are more closely related to the solution. This is an area for future work.

5.2. Flow past a cylinder

The second benchmark problem that we consider involves steady, laminar flow past a right circular cylinder. We consider a domain of height h and width w containing a circular obstacle of diameter d (Fig. 10). The boundary conditions for the hypertraction $\mathbf{m}_\mathscr{S}$ and the horizontal and vertical components u and v of the velocity field are indicated in the figure. On the cylinder surface, no-slip conditions are considered along with generalized adherence boundary conditions ($l > 0$). A uniform velocity in the x-direction at the inlet boundary is applied. The computational domain is taken as $h/w = 1$, and $h/d = 4$. We find that the mesh shown in Fig. 11 of 288 quadratic elements provides sufficiently converged results for all of the problems presented below.

Fig. 12 compares numerical approximations for the horizontal component of the velocity field for the classical Navier–Stokes theory and the gradient theory. The results correspond to generalized adherence boundary conditions ($l > 0$) on the cylinder surface, with $L/d = 1.0$ and $l/L = 10.0$. The two solutions are seen to be qualitatively quite similar, with perhaps the greatest difference occurring in the vicinity of the cylinder. This is not surprising given the generalized adherence condition there.

Fig. 13 displays contour plots of the vertical component of the velocity field for the classical Navier–Stokes theory and the gradient theory. Only minor qualitative and quantitative differences between the two flows can be observed, but the adherence near the cylinder boundary is clearly identifiable. Fig. 14 shows the pressure distributions for the classical (left) and gradient (right) flows. As expected, these results show a pressure drop as the flows pass the cylinder. Moreover, we find that the pressure field upstream of the cylinder for the gradient theory is greater than that predicted by the classical theory.

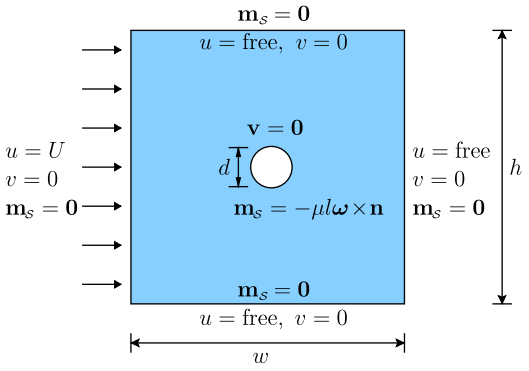

Fig. 10. Problem description for flow past a cylinder with velocity and hypertraction boundary conditions.

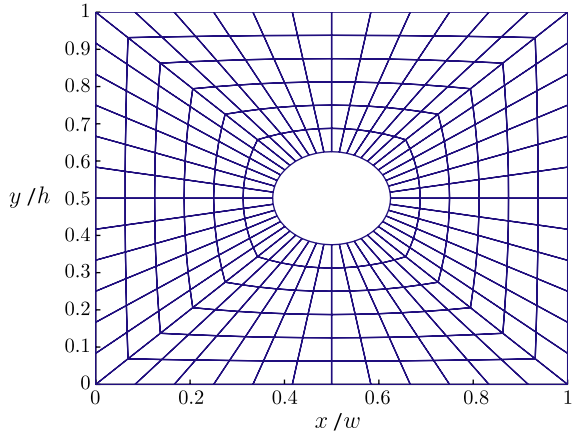

Fig. 11. Mesh for studies of flow past a cylinder.

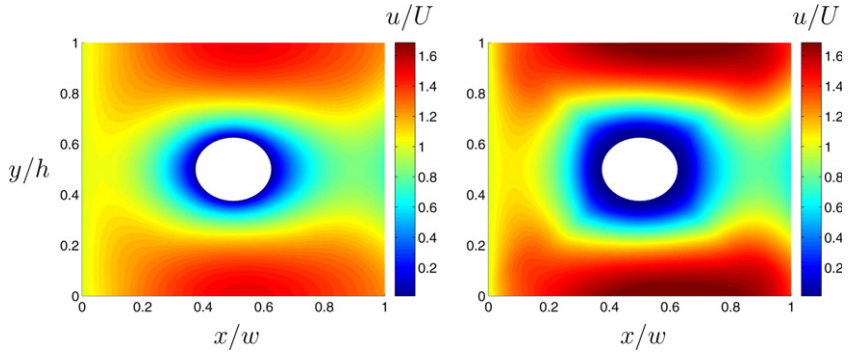

Fig. 12. Contour plots of the normalized horizontal velocity component for the classical theory (left) and the gradient theory (right) with generalized adherence boundary conditions. Results for the gradient theory correspond to $L/d = 1.0$ and $l/L = 10.0$.

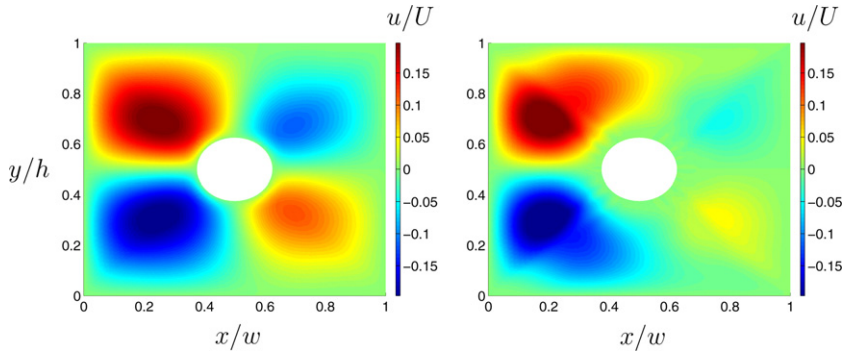

Fig. 13. Contour plots of the normalized vertical velocity component for the classical solution (left) and the gradient (right) solution with generalized adherence boundary conditions. Results for the gradient theory correspond to $L/d = 1.0$ and $l/L = 10.0$.

Fig. 15 compares the horizontal velocity components for the classical theory with those of weak- and generalized-adherence boundary conditions under the gradient theory. The numerical results correspond to the flow profiles along a vertical line along the middle ($x/h = 0.5$) of the computational domain. All of the numerical results shown in the figure were obtained using a mesh of 288 elements. The results indicate that

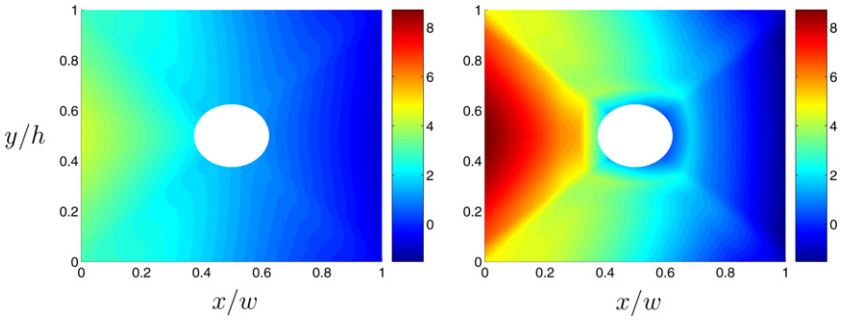

Fig. 14. Contour plots of pressure field for the classical solution (left) and the gradient (right) solution with generalized adherence boundary conditions.

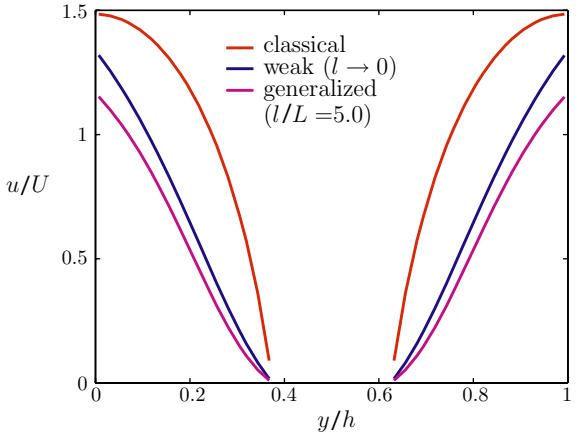

Fig. 15. Comparison of the normalized horizontal velocity component profiles in the middle ($x/w = 0.5$) of the computational domain for the classical theory and weak- and generalized-adherence boundary conditions on the cylinder surface with the gradient theory.

the velocity profiles at small length scales are smaller than those of classical theory. Moreover, the slope around the cylinder decreases with increasing gradient and adherence lengths (L and l).

5.3. Step flow

We consider a steady, laminar flow through a channel with a sudden area expansion as shown in Fig. 16. We prescribe a pressure drop $-P$ between the inlet and outlet boundaries as shown in the figure. The vertical component of the velocity field is also fixed to zero at the inlet and outlet boundaries. On the top and bottom surfaces, no-slip boundary conditions are enforced, and weak adherence ($l = 0$) conditions are considered for

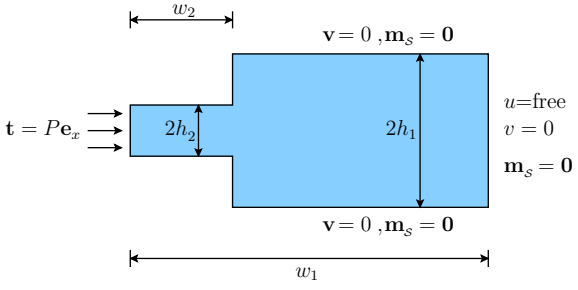

Fig. 16. Geometry and boundary conditions for the step flow problem. The coordinates in the directions downstream and out of the plane are x and z.

the gradient theory. The dimensions of the computational domain are taken such that $w_1/w_2 = 3$, $h_1/h_2 = 5/2$, and $h_1/w_1 = 5/6$.

Figs. 17 and 18 provide contour plots of the numerical solution of the horizontal and vertical velocity components for classical (left) and gradient (right) flows. The numerical results were obtained using a uniform mesh of 176 elements. As expected, the results reveal a qualitative difference between classical and gradient theories. Fig. 19 provides the pressure comparison at the same contour level between classical and gradient theories. The results clearly show the same net pressure drop between inlet and outlet boundaries. A profile of the horizontal velocity field at the outlet of the computational domain is shown in Fig. 20. The gradient

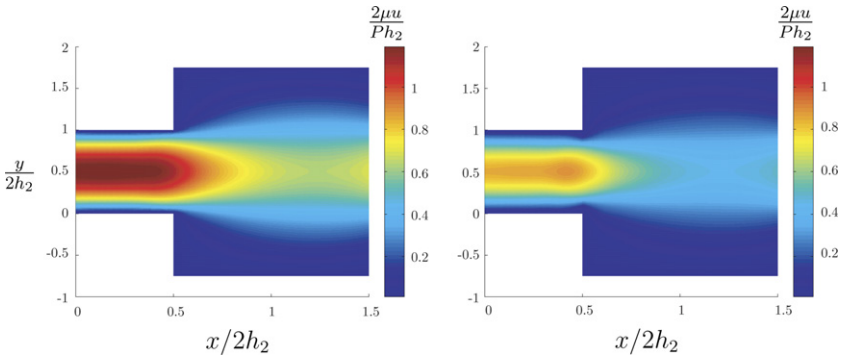

Fig. 17. Contour plot of normalized horizontal velocity component predicted using the classical theory (left) and the gradient theory (right) with weak adherence boundary conditions.

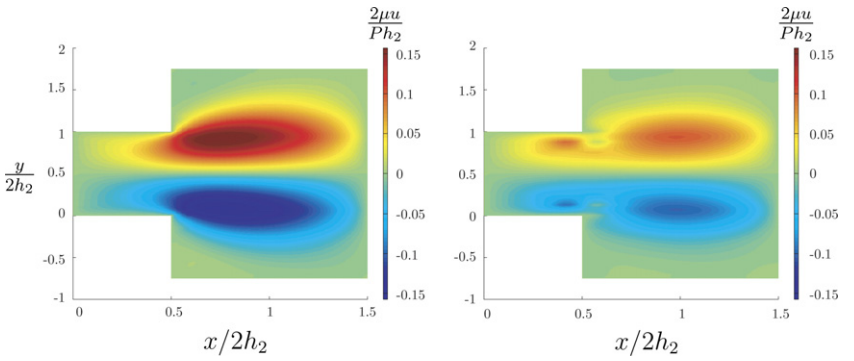

Fig. 18. Contour plot of vertical velocity component for the classical solution (left) and the gradient (right) solution with weak adherence boundary conditions.

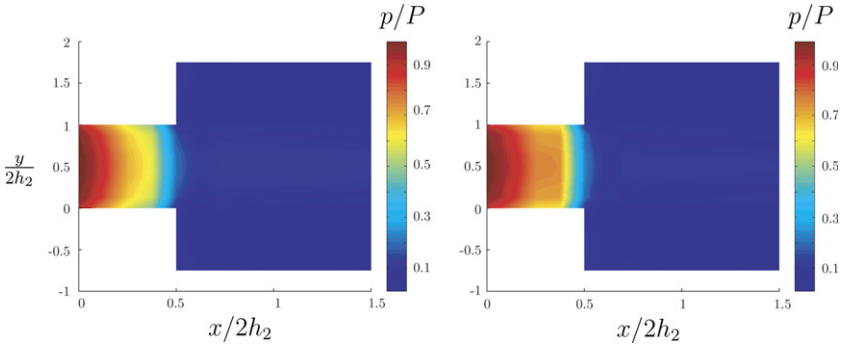

Fig. 19. Contour plot of normalized pressure fields for the classical (left) and gradient (right) theories for the step flow problem.

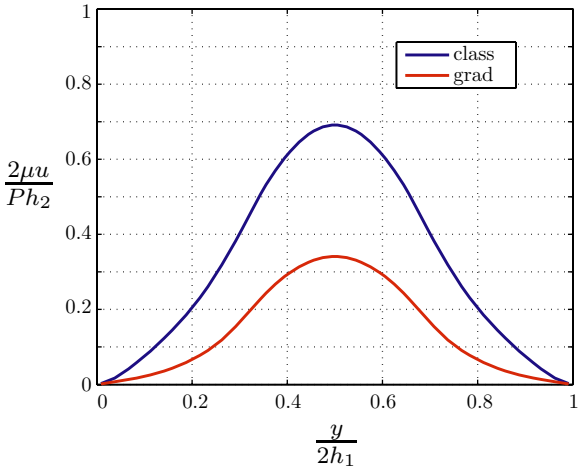

Fig. 20. Normalized horizontal velocity profiles at the outlet of the computational domain for the classical theory and the gradient theory for the step flow problem.

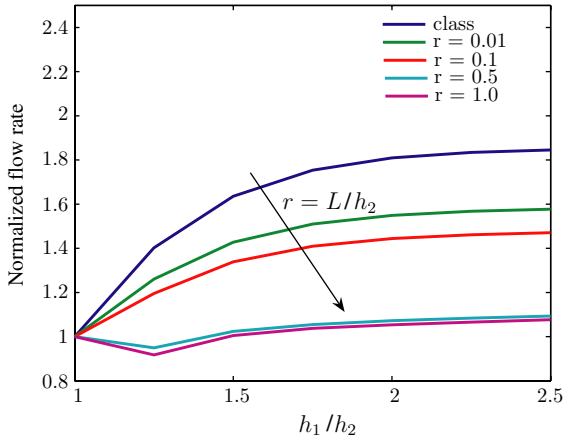

Fig. 21. Normalized flow rates as a function of step ratio h_1/h_2 for a sequence of increasing ratios L/h_2 of gradient to physical lengths.

theory clearly predicts smaller flow rates compared to the classical for the same pressure drop across the step. The results for the gradient theory shown in Figs. 17–20 were all obtained using $L/h_2 = 0.25$.

We next examine the variation in flow rates with aspect ratio h_1/h_2 for a fixed pressure drop. We calculate the flow rates Q for a sequence of steps ranging from $h_1 = h_2$ (the straight channel) to $h_1 = 2.5h_2$. We use the flow rate Q_1 obtained for the straight channel in each case (classical and gradient) to normalize the subsequent results. Fig. 21 shows the normalized flow rates as a function of step ratio h_1/h_2 for a sequence of increasing ratios L/h_2 of gradient to physical lengths. The results predict that the flow rate of the classical theory is always greater than that of the gradient theory. Moreover, flow rates are seen to decrease relative to the straight channel rate as the gradient length is increased relative to the physical length. We note that the introduction of the corner to the problem results in a marked decrease in flow rates (before a more gradual increase with increasing step size) for large L/h_2. This may be attributable to the increased role that corner singularities may play with regard to dissipation for the gradient theory.

6. Summary and conclusions

In this paper, we described a finite-element method for a second-gradient theory of fluid flow. The second gradient theory incorporates gradients of the vorticity field that are power-conjugate to a hyperstress in a

non-standard principle of virtual power. The theory gives rise to a flow equation that is fourth-order in the velocity field, and incorporates associated higher-order boundary conditions. Rather than employing C^1-continuous basis functions or a fully mixed approach, we base our method on a recent formulation for fourth-order elliptic problems that employs C^0-continuous basis functions. Continuity of higher-order velocity derivatives is then enforced between elements using a variation of Nitsche's [11] method, involving jump quantities across interelement boundaries. Using this formulation, we based our approach on second-order elements that are stable for the classical Navier–Stokes theory for incompressible fluid flow. Additional terms were added to properly stabilize the discontinuous pressure field.

Using our finite-element method, we then examined several numerical examples. First, the method was verified using an analytical solution to a Poiseuille flow problem derived by Fried and Gurtin [4]. An excellent match between numerical and analytical results was obtained, as were near-optimal rates of convergence in appropriate error norms for the velocity and pressure fields. The numerical method was also shown capable of capturing effects for a range of boundary conditions stemming from the second-gradient theory, from weak to strong adherence. Results were obtained using stabilization parameters that scale with the second-gradient moduli and the inverse of the mesh spacing. Additional problems of flow past a cylinder and step flow were then examined, and numerical predictions based on the second-gradient theory were compared to those of the classical theory. Consistent with the additional sources of dissipation associated with the hyperstress and the generalized adherence boundary conditions, the second-gradient theory predicts lower flow rates and shows a marked difference near boundaries due to the effect of the adherence boundary conditions.

This work is based on a theory of fluid flow that involves the gradient of the vorticity field [5]. It shares several common features with an earlier theory based on the full second-gradient of the velocity field [4]. The earlier theory involves an additional hyperpressure field not present in the vorticity-based theory considered here. A numerical formulation based on the earlier theory would thus require a three-field approach for which it would be more difficult to ensure stability. Since both theories yield identical flow equations, however, we do not anticipate significant qualitative differences in the flow profiles.

A drawback to the current method is the need to identify suitable parameters τ_v and τ_p for the velocity and pressure stabilization, respectively. As the method is relatively new, closed-form expressions are not currently available and for a given simulation there exists a range of both parameters that will yield accurate results. Accordingly, we intend to examine methods that can better tie the stabilization parameters to the solution in a particular problem. Along these lines, Mourad et al. [22] have recently developed a method to relate the stabilization parameters in Nitsche's [11] method to the relationship between coarse and fine scales in a solution. In principle, such a strategy could be applied to the present work, provided that a suitable approximation for the fine-scale can be identified.

Future work will focus on extending our approach to time-dependent flows beyond the steady Stokes flows considered herein. This work should serve as an excellent starting point for a formulation based on the generalization of the LANS-α theory for turbulent flow obtained by Fried and Gurtin [5], for example.

Acknowledgment

The support of the Department of Energy to Duke University and Washington University is gratefully acknowledged.

References

[1] M.E. Gurtin, A gradient theory of single-crystal viscoplasticity that accounts for geometrically necessary dislocations, J. Mech. Phys. Solids 84 (2001) 809–819.
[2] R.A. Toupin, Elastic materials with couple stresses, Arch. Ration. Mech. Anal. 11 (1962) 385–414.
[3] R.A. Toupin, Elastic materials with couple stresses, Arch. Ration. Mech. Anal. 17 (1964) 85–112.
[4] E. Fried, M.E. Gurtin, Tractions, balances, and boundary conditions for nonsimple materials with application to liquid flow at small length scales, Arch. Ration. Mech. Anal. 182 (2006) 513–554.
[5] E. Fried, M.E. Gurtin, Cosserat fluids and the continuum mechanics of turbulence: a generalized Navier–Stokes-α equation with complete boundary conditions, submitted for publication.

[6] D.D. Holm, C. Jeffrey, S. Kurien, D. Livescu, M.A. Taylor, B.A. Wingate, The LANS-α model for computing turbulence: origins, results, and open problems, Los Alamos Science 29 (2005) 152–171.
[7] J. Petera, J.F.T. Pittman, Isoparametric hermite elements, Int. J. Numer. Meth. Eng. 37 (1994) 3489–3519.
[8] M. Fortin, F. Brezzi, Mixed and Hybrid Finite Element Methods, Springer, New York, 1991.
[9] G. Engel, K. Garikipati, T.J.R. Hughes, M.G. Larson, L. Mazzei, R.L. Taylor, Continuous/discontinuous finite element approximations of fourth-order elliptic problems in structural and continuum mechanics with applications to thin beams and plates, and strain gradient elasticity, Comput. Meth. Appl. Mech. Eng. 191 (2002) 3669–3750.
[10] T.J.R. Hughes, The Finite Element Method, Dover Publications, New York, 1987.
[11] J.A. Nitsche, Über ein Variationsprinzip zur Lösung von Dirichlet-Problemen bei Verwendung von Teilräumen, die keinen Randbedingungen unterworfen sind, Abhandlungen aus dem Mathematischen Seminar der Universität Hamburg 36 (1970/71) 9–15.
[12] I. Babuška, The finite element method with penalty, Math. Comp. 27 (1973) 221–228.
[13] J. Dupont Jr., T. Dupont, Interior Penalty Procedures for Elliptic and Parabolic Galerkin MethodsLecture Notes in Physics, vol. 58, Springer-Verlag, Berlin, 1976.
[14] F. Bassi, S. Rebay, A high-order accurate discontinuous finite element method for the numerical solution of the compressible Navier–Stokes equations, J. Comp. Phys 131 (1997) 267–279.
[15] F. Brezzi, G. Manzini, D. Marini, P. Pietra, A. Russo, Discontinuous Galerkin methods for elliptic problems, Numer. Meth. Partial Differ. Equations 16 (2000) 365–378.
[16] K.S. Bey, J.T. Oden, hp-version discontinuous Galerkin methods for hyperbolic conservations laws, Comput. Meth. Appl. Mech. Eng. 133 (1996) 259–286.
[17] B. Cockburn, C.W. Shu, The local discontinuous Galerkin finite element method for convective–diffusion systems, SIAM J. Numer. Anal. 35 (1998) 2440–2463.
[18] C.E. Baumann, An hp-adaptive discontinuous finite element method for computational fluid dynamics, Ph.D. thesis, The University of Texas at Austin, Austin, TX, 1997.
[19] T.J.R. Hughes, L.P. Franca, A new finite element formulation for computational fluid dynamics: VII, Comput. Meth. Appl. Mech. Eng. 65 (1987) 85–96.
[20] T.J.R. Hughes, L.P. Franca, M. Balestra, A new finite element formulation for computational fluid dynamics: V. Circumventing the Babuska–Brezzi condition: a stable Petrov–Galerkin formulation of the Stokes problem accommodating equal-order interpolations, Comput. Meth. Appl. Mech. Eng. 59 (1986) 85–99.
[21] J.G. Heywood, S. Rannacher, S. Turek, Artificial boundaries and flux and pressure conditions for the incompressible Navier–Stokes equations, Int. J. Numer. Meth. Fluids 22 (1996) 325–352.
[22] H.M. Mourad, J. Dolbow, I. Harari, A bubble-stabilized finite element method for Dirichlet constraints on embedded interfaces, Int. J. Numer. Meth. Eng., in press.